



Thermal and Nonthermal Emissions of a Composite Flare Derived from NoRH and *SDO* Observations

Jeongwoo Lee^{1,2} , Stephen M. White³ , Ju Jing⁴ , Chang Liu⁴ , Satoshi Masuda², and Jongchul Chae¹ 

¹Department of Physics and Astronomy, Seoul National University, Seoul 08826, Korea; leej@astro.snu.ac.kr

²Institute for Space-Earth Environmental Research, Nagoya University, Aichi 464-8601, Japan

³Air Force Research Laboratory, Space Vehicles Directorate, Albuquerque, NM 87117, USA

⁴Space Weather Research Laboratory, New Jersey Institute of Technology, Newark, NJ 07102, USA

Received 2017 August 25; revised 2017 October 23; accepted 2017 October 26; published 2017 November 27

Abstract

Differential emission measure (DEM) derived from the extreme ultraviolet (EUV) lines of the *Atmospheric Imaging Assembly* (AIA) on board the *Solar Dynamic Observatory* is used in the analysis of a solar flare observed by the Nobeyama Radioheliograph (NoRH). The target was a composite event consisting of an impulsive flare, SOL2015-06-21T01:42 (*GOES* class M2.0), and a gradual flare, SOL2015-06-21T02:36 (M2.6), for which separation of thermal plasma heating from nonthermal particle acceleration was of major interest. We have calculated the thermal free–free intensity maps with the AIA-derived DEM and compared them against the observed NoRH maps to attribute the difference to the nonthermal component. In this way, we were able to locate three distinct sources: the major source with thermal and nonthermal components mixed, a nonthermal source devoid of thermal particles, and a thermal source lacking microwave emission. Both the first and the second nonthermal sources produced impulsively rising 17 GHz intensities and moved away from the local magnetic polarization inversion lines in correlation with the flare radiation. In contrast, the thermal sources stay in fixed locations and show temporal variations of the temperature and emission measure uncorrelated with the flare radiation. We interpret these distinct properties as indicating that nonthermal sources are powered by magnetic reconnection and thermal sources passively receive energy from the nonthermal donor. The finding of these distinct properties between thermal and nonthermal sources demonstrates the microwave and EUV emission measure combined diagnostics.

Key words: methods: data analysis – Sun: activity – Sun: corona – Sun: flares – Sun: radio radiation

1. Introduction

The magnetic energy released during solar flares is imparted to particles in the form of either thermal heating or nonthermal particle acceleration. The relationship between these two components is an important constraint on flare mechanisms. One method for addressing this question employs joint fitting of the thermal and nonthermal spectral components in X-ray spectra. This method requires high spectral resolution together with wide photon energy coverage, and the *Reuven Ramaty High Energy Solar Spectroscopic Imager* (RHESSI) has provided data for a number of such studies. The success of these studies largely depends on the sensitivity limit of the X-ray instrument, because separation of the two components in the spectral domain depends critically on the signal-to-noise in the spectra (cf. Saint-Hilaire et al. 2011). In particular, the total energy in nonthermal electrons is largely controlled by the low-energy cutoff in a power-law distribution, and it is very difficult to determine this from hard X-ray (HXR) spectra, where it is often masked by thermal emission.

Similarly, microwave imaging spectroscopy during solar flares can also be used, since microwave emission contains contributions from both thermal (via free–free emission) and nonthermal (via gyrosynchrotron) electrons (Dulk 1985). Microwave spectroscopic observation may offer higher sensitivity to energetic electrons than X-ray spectroscopy, depending on the magnetic field strength in the source. But the inversion of the microwave spectrum to derive energetics can be more complicated because the gyrosynchrotron emission also depends on magnetic field strength (e.g., Dulk &

Marsh 1982). When either entirely thermal or entirely nonthermal spectra are observed with sufficiently high spectral resolution, a simple inversion may be possible (see, for instance, Gary & Hurford 2004). Otherwise, both thermal and nonthermal electrons coexist and can be analyzed by forward modeling for a homogeneous source with an integrated spectrum (Benka & Holman 1992) or an inhomogeneous source with imaging spectroscopy (Gary et al. 2013).

In this paper, we test a new method for determining thermal and nonthermal components in microwave maps that can be performed without hard X-ray imaging spectroscopy. This method employs high-sensitivity, high-fidelity microwave images along with emission measure (EM) data in the temperature range matching the hot corona present in flares. Another important requirement is that the microwave radiation at the observing frequency should be optically thin, which is more likely to be the case at higher frequencies (e.g., ≥ 17 GHz). The Nobeyama Radioheliograph (NoRH) provides these characteristics and is the most suitable instrument for such a test. The idea is to initially focus on the contribution of free–free (f–f) emission that can be calculated simply with knowledge of the EM and temperature (T) only. Once the f–f emission is calculated and subtracted from the observed flux, we should be able to separate out the nonthermal component and analyze it on its own. In the presence of an inhomogeneous temperature distribution, EM as a function of T or the differential emission measure (DEM) distribution provides sufficient information to predict the thermal f–f radio emission. Such DEM inversions can now be performed on narrowband extreme ultraviolet (EUV) images from the *Atmospheric*

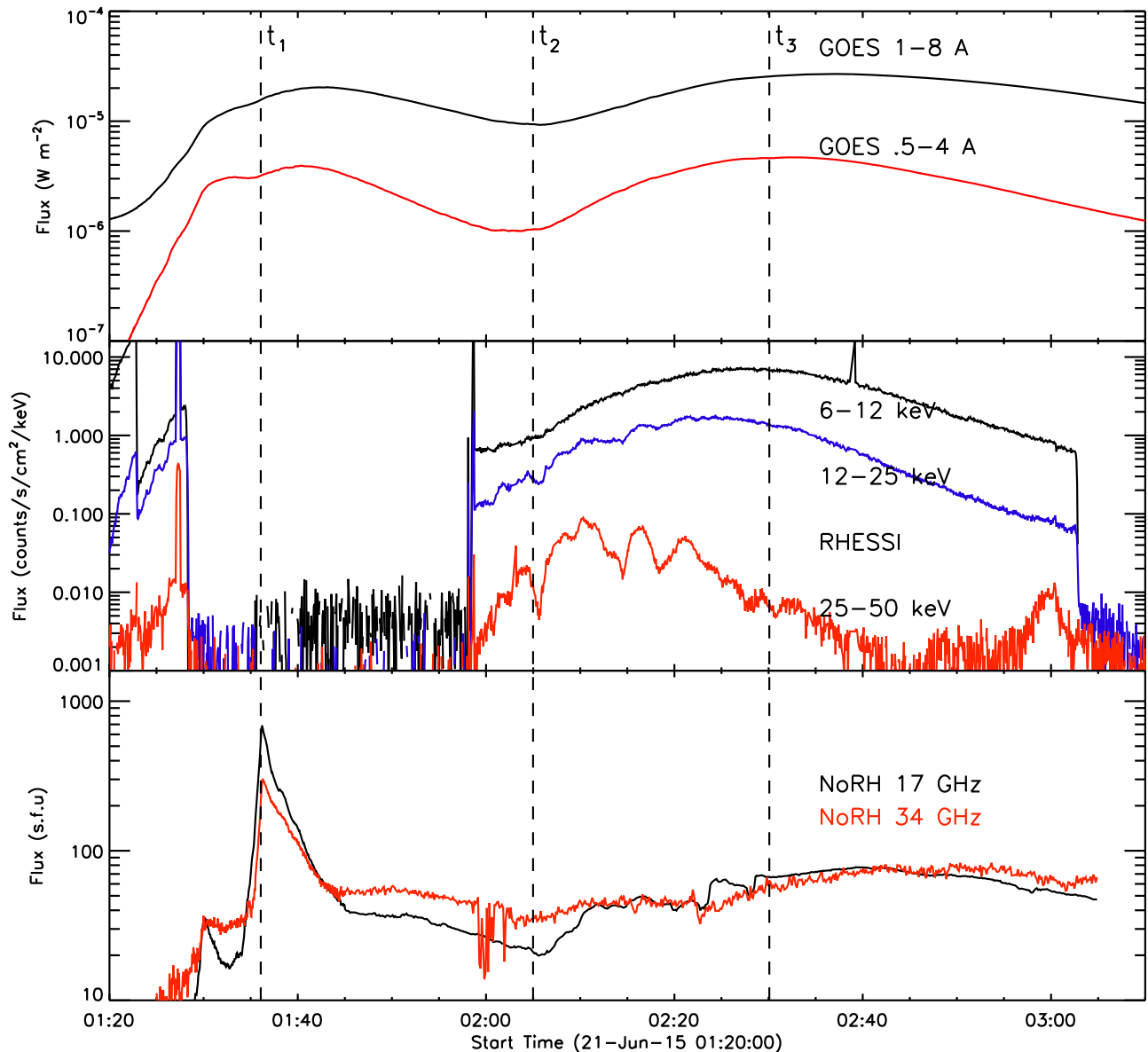


Figure 1. Soft X-ray light curves from *GOES* (top), *RHESSI* light curves (middle), and microwave fluxes from the NoRH maps (bottom). The vertical dashed lines mark three time points, t_1 – t_3 , corresponding to the first flare peak, an intermission, and the second flare peak set based on the *GOES* 0.5–4 Å light curve.

Imaging Assembly (AIA; Boerner et al. 2012; Lemen et al. 2012) instrument on board NASA’s Solar Dynamics Observatory (*SDO*; Pesnell et al. 2012). A combination of NoRH data and AIA EM data will therefore be the most ideal tool for this application.

The plan of this paper is as follows. In Section 2, we describe the event and state the motivation. Our method is introduced in Section 3, including the abundance issue and the result of the *SDO/AIA* analysis. We discuss the location of nonthermal sources in Section 4 and identify thermal/nonthermal structures in Section 5. We present the temporal evolution of temperature and EM in Section 6 and conclude in Section 7.

2. Event Description and Motivation

The target of this study is a set of two consecutive flares on 2015 June 21 with the *Geostationary Operational Environmental Satellite* (*GOES*) class M2.0 and M2.6 flares, respectively. Figure 1 shows the light curves of the *GOES*

soft X-rays, the *RHESSI* hard X-rays, and the microwave fluxes computed from the NoRH maps. We use the peak times of the *GOES* 1–8 Å fluxes to denote the two flares as SOL2015-06-21T01:42 and SOL2015-06-21T02:36. We also mark (vertical dashed lines) three time points corresponding to the first flare peak ($t_1 = 01:36$ UT), an intermission ($t_2 = 02:05$ UT), and the second flare peak ($t_3 = 02:30$ UT) based on the *GOES* 0.5–4 Å light curve to be used for the display of images in Figures 3–5. In terms of the *GOES* light curves, the two peaks are of comparable duration, but in the NoRH time profiles, the first is impulsive and the second is gradual; this is dubbed a “composite” flare (Kosugi et al. 1988). Since these two temporal behaviors are generally associated with nonthermal and thermal electrons, respectively (e.g., Dulk 1985), the contrast between the two events is intriguing, and one of our tasks is to separate the two components through other observational data and compare them for each flare. *RHESSI* missed the impulsive phase of the first flare around 01:36 UT, and the fluxes measured subsequently are relatively low, so that

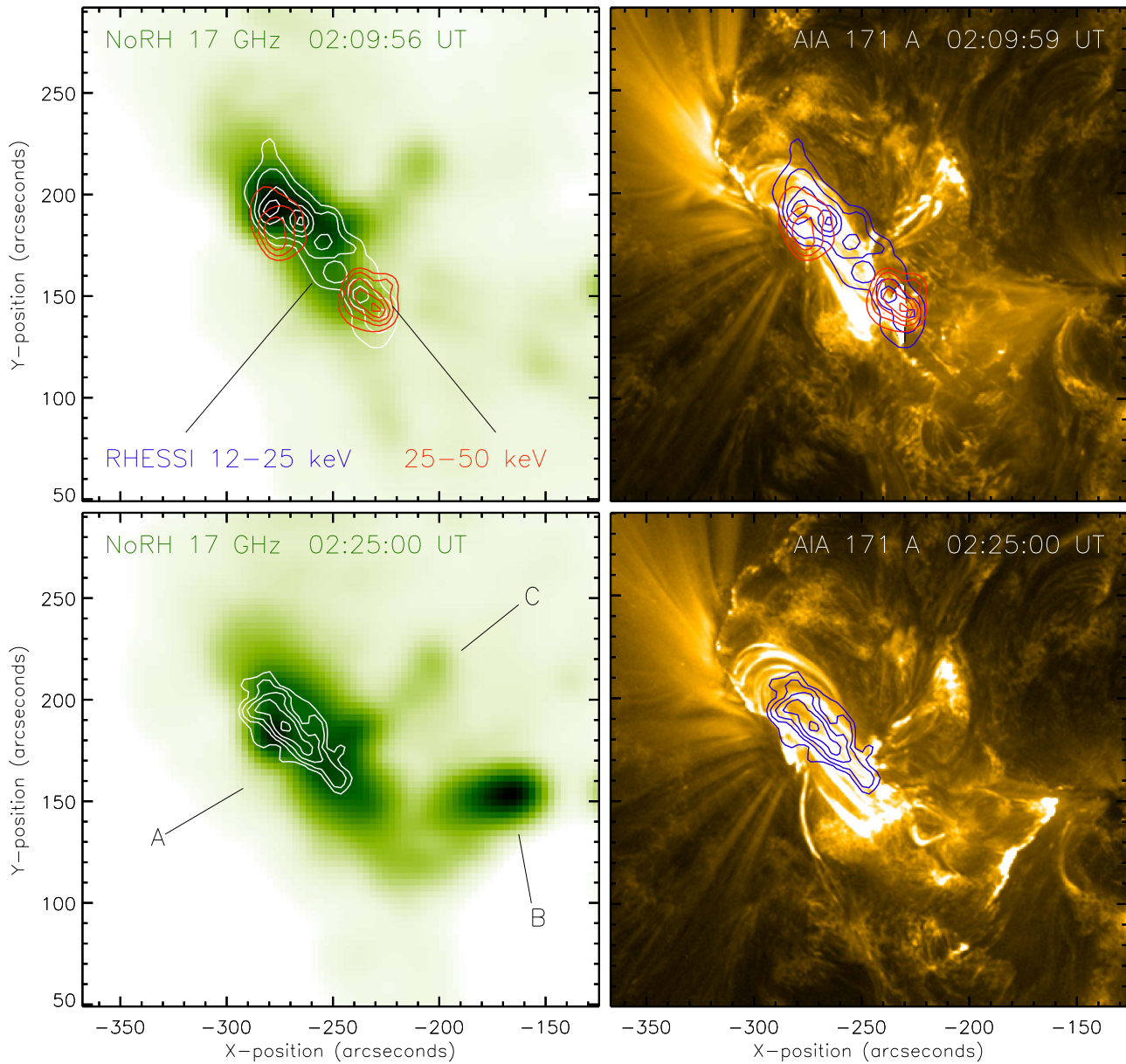


Figure 2. *RHESSI* sources on the NoRH maps (left panels) and AIA 171 Å maps (right panels). *RHESSI* maps in the specified energy bands are constructed using the pixion method at the time interval of the highest flux at 25–50 keV (02:09:56–02:10:32 UT; upper panels) and that at 12–25 keV (02:25:00–02:27:00 UT; lower panels). The *RHESSI* contour levels are 10%, 17%, 30%, 52%, and 90% of the maximum intensity on each map. The 12–25 eV contours are colored white in the left panels and blue in the right panels for visibility. Three NoRH sources are denoted as A to C (see the text for details).

imaging at high energies (say, ≥ 25 keV) is not possible except around t_2 . We also note that these *RHESSI* light curves are contaminated by unidentified variable particle fluxes, which makes spectral analysis challenging in this case.

Figure 2 shows the *RHESSI* sources constructed using the pixion method at two energy intervals (contours) overlaid on the NoRH 17 GHz maps (left panels) and the AIA 171 Å maps (right panels). Maps in the upper panels are constructed in the time interval of the highest flux at 25–50 keV (02:09:56–02:10:32 UT), and the bottom panels show the period of the highest flux at 12–25 keV (02:25:00–02:27:00 UT). On the bottom NoRH 17 GHz map, we denote three sources as A–C. The 17 GHz source B appears after $\sim 02:20$ UT and reaches its maximum flux at around t_3 . At the second time interval, *RHESSI* imaging could not be made up to the 25–50 keV energy band and higher. Note that all 17 GHz sources have counterparts on EUV maps but not

necessarily on hard X-ray maps. Only A is detected by *RHESSI*; although the *RHESSI* sources appear in multiple compact structures, they generally line up along A. Source B is a very strong source at 17 GHz but dim at EUV and unseen by *RHESSI*. The EUV-dim microwave source can be explained if B has mostly nonthermal electrons but lacks thermal particles. The absence of a *RHESSI* source over B implies that B does not offer a favorable condition for X-ray bremsstrahlung, although it has nonthermal electrons emitting synchrotron radiation. This is possible when the density of cold particles in B is too low to make sufficient Coulomb collisions with nonthermal electrons. The absence of an X-ray source at C can be understood if C lacks nonthermal electrons, even though a large number of thermal particles is available. This is not a surprising result, because it is common that not all EUV-bright regions are accompanied by either hard X-ray or microwave sources.

It is our goal to verify the nature of the three sources. *RHESSI* sources are likely confined to the regions of intense precipitation of nonthermal electrons, and, with limited dynamic range in the images, it is unable to fully reveal all locations where significant nonthermal electrons are present. In contrast, the NoRH 17 GHz maps faithfully reproduce the EUV thermal features and additionally reveal nonthermal components superimposed on them. This sensitivity makes the combination of microwave and EUV diagnostics a potentially powerful tool for studying energy distributions in weak sources.

We also check *GOES* soft X-ray data. *GOES* data carry information on thermal particles like that of *AIA* and can be used to cross-check our *AIA* result. However, *GOES* provides only a single value of T and EM, both of which represent the whole Sun and the entire temperature range to which it is sensitive. Unless both instruments have an identical temperature sensitivity, *GOES* and *AIA* may yield different information on thermal particles, which is another issue to be investigated.

3. Method

3.1. Calculation of f–f Emission

With $EM(T)$ determined for a wide range of coronal temperature, we can completely determine the thermal f–f opacity as given by (Melrose 1980; Schonfeld et al. 2015)

$$\tau \approx 9.78 \times 10^{-3} \frac{EM(T)}{\nu^2 T^{3/2}} \left(1 + 4 \frac{n_{\text{He}}}{n_{\text{H}}} \right) (24.5 + \ln T - \ln \nu), \quad (1)$$

where ν is the frequency in Hz, $n_{\text{He}}/n_{\text{H}} = 0.085$ (Asplund et al. 2009) is the number density ratio of helium to hydrogen in the emitting medium, and $EM(T)$ is the integral of n_e^2 along the line of sight through the corona, where n_e is electron density (Dulk & Marsh 1982). Analysis of the *AIA* data returns $EM(T)$ for specified temperature intervals, and we integrate this expression over the whole temperature range to obtain total radio fluxes due to f–f emission. In contrast, NoRH gives spatially resolved images with units of brightness temperature, which is $T_b \approx \tau T$ for optically thin radiation, where T is the actual temperature in the source. This approximation is justified only when the radiation is optically thin. Fortunately, we are dealing with high frequencies ≥ 17 GHz during a flare period when $\langle T \rangle \approx 1.0 \times 10^7$ K, in which case the optically thin condition reduces to the requirement $EM < 5 \times 10^{31} \text{ cm}^{-5}$, which is well satisfied in the present case (see Figure 3).

3.2. Abundances

In any quantitative comparison of *AIA*-derived EMs and radio data, the issue of relative abundances must be addressed. The coronal *AIA* bandpasses are designed to be dominated by lines of Fe, so the total coronal EMs reported from analysis of *AIA* data require an assumption about the abundance [Fe/H]. The *AIA* temperature-response functions are calculated assuming ‘‘coronal’’ abundances (based predominantly on EUV and soft X-ray (SXR) spectroscopy, as well as solar-wind measurements; Feldman 1992), in which [Fe/H] is 4 times the value of [Fe/H] in the photosphere. This value is supported for active regions by a direct measurement of [Fe/H] in which

EUV spectroscopy was used to determine the EM of Fe, while radio measurements of bremsstrahlung emission were simultaneously used to derive the coronal EM of H (White et al. 2000). Widing & Feldman (2001) found that newly emerged active regions can have photospheric abundances in the corona at first, developing coronal abundances over a few days, but all the active regions studied by Schonfeld et al. (2015) were consistent with a coronal value of [Fe/H]. In this paper, we investigate a flare, and the appropriate abundance to use is not as clear. Much of the coronal emission from flares is believed to come from chromospheric material that has just been heated by electron beams, and there is no reason to assume that it will instantaneously attain coronal abundances. Flares have the advantage that continuum due to H is often strong enough to be measured at SXR and EUV wavelengths, so direct measurements of [Fe/H] are possible spectroscopically. Fludra & Schmelz (1999) studied 57 flares and argued for a hybrid abundance in which [Fe/H] is about twice the photospheric value (see also Schmelz et al. 2012), while Phillips et al. (2010) concluded that 4 times photospheric was appropriate for their sample of 19 flares. We proceed with the analysis of *AIA* flare data here using the default temperature responses that assume [Fe/H] that is 4 times photospheric while bearing in mind the fact that if hybrid abundances are more appropriate, the bremsstrahlung radio fluxes derived from the *AIA* data will be twice the values that we discuss here.

3.3. EUV EM Maps

We follow the procedure developed by Cheung et al. (2015), which uses *AIA* instrument response data structures from the six EUV coronal channels (94, 131, 171, 193, 211, and 335 Å) in order to derive $DEM(T) \Delta T = \int_0^\infty n_e^2(T) dz$, where n_e is in cm^{-3} and T is in K; $\int dz$ refers to the line-of-sight integration. We used the dark-subtracted, flat-fielded, and exposure time-normalized count rate in the i th EUV channel and fit over 20 uniformly spaced (in $\log T$) intervals in the range of $5.7 \leq \log T \leq 7.7$. The procedure returns EM integrated over each temperature interval in units of $[\text{cm}^{-3}]$. We perform the *AIA* analysis throughout the period from 01:25 UT to 03:05 UT; the NoRH data were obtained every 2 s, and those close to the measurement times of the *AIA* data are used.

Figure 3 shows the maps of the *AIA*-derived $EM(T)$ in the scale denoted by the color bars at two selected temperature intervals and three selected time points, t_1 – t_3 , as marked in Figure 1. There is a general trend that the EM has a narrow spatial distribution in the lowest temperature range, $5.75 \leq \log T < 6.05$, but is significantly more extended in the higher temperature at $6.65 \leq \log T < 6.95$. The width and area of the high-EM regions increase with time after the flare, which can be regarded as the spatial Neupert effect (Neupert 1968).

From now on, we focus on three local sources, as marked by the boxes in the upper right panel of Figure 3: source A enclosing the eastern spot, B near the western spot, and C at a prominent EUV source in the southwest. Source A dominates throughout the whole event, as it has the largest amount of EM at all times. Its temporal evolution, therefore, matches the time profiles of the *GOES* soft X-ray light curves. To the north of A, we find a prominent loop and an extruding structure at t_2 that is regarded as the hot plasma ejection from the active region toward a coronal hole located to the east. Source B is a

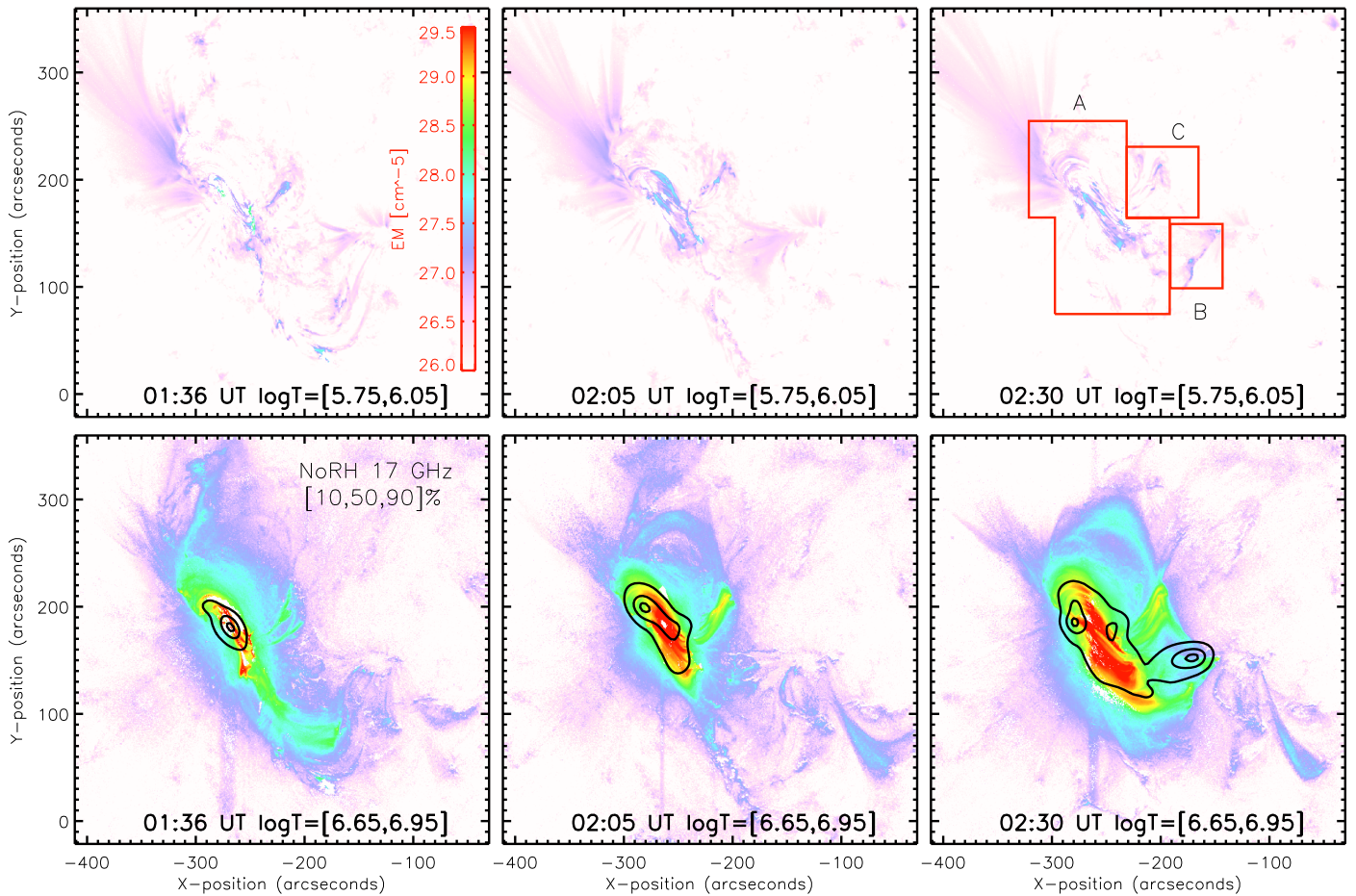


Figure 3. Maps of $EM(T)$ in two temperature intervals (upper and lower panels) determined from *SDO/AIA* lines at three time points, t_1 – t_3 (left to right). The bottom panels include the NoRH 17 GHz maps at the nearby times as black contours. The three sources defined in Figure 2 are marked here with boxes.

significant microwave source after $\sim 02:10$ UT but is never bright at EUV wavelengths. Only after t_2 does a faint EUV structure appear, outlining a semicircular UV ribbon. This implies that source B may be filled with nonthermal electrons and is largely void of thermal plasma. In contrast, C is never bright in microwaves but is very bright in EUV. This source must be filled with thermal plasma lacking nonthermal electrons.

4. Locations of Nonthermal Electrons

We calculate the thermal brightness temperature T_b^T using the *AIA*-derived $EM(T)$ over all the temperature bins (two of which are presented in Figure 3) and compare with the observed T_b , which includes the nonthermal brightness temperature $T_b^{NT} = T_b - T_b^T$. Figure 4 shows the NoRH 17 GHz maps as contours on the *SDO/AIA* 171 Å images (top panels) and the thermal and nonthermal brightness temperatures on the Helioseismic and Magnetic Imager (HMI) magnetogram (bottom panels) at three time intervals (t_1 – t_3). The *AIA*-derived T_b^T maps are convolved with a Gaussian beam of width $10''$ in order to match the spatial resolution of the NoRH 17 GHz maps.

The first panel shows that the NoRH source at t_1 is a single compact source located above the magnetic polarization inversion line (PIL) of the eastern bipolar spot. Some thermal emission is also present but is much weaker, so the difference

intensity, $T_b - T_b^T$, (red contours in the bottom left panel) not significantly different from T_b in the top left panel. We thus conclude that the 17 GHz emission at t_1 is dominated by nonthermal gyrosynchrotron emission.

In the middle column (t_2), the emission extends to the south and also to the western unipolar spot. The elongation of the thermal source along the north–south direction can be attributed to thermalization of plasma trapped in the sheared magnetic loops along the PIL. There is another component extruding from the PIL to the northwest that is bright in the *AIA* 171 Å image (top middle panel) but dim in the 17 GHz image (bottom middle panel), implying that it is a thermal source. The subtracted image (red contours) does not look very different from the observed one (black contours) but has two sources across the PIL that are more clearly distinguishable, which is more like a two-ribbon structure common to H α observations.

In the right column (t_3), another radio source suddenly appears in region B where no strong EUV or 17 GHz emission was previously present. This source does not lie over the western spot but rather between the two spots. Underneath this new 17 GHz source, a semicircular EUV ribbon forms and progressively moves toward the western spot. Since the region is void of *AIA* EM, we regard this 17 GHz source as an almost entirely nonthermal source. In contrast, A was initially nonthermal and becomes a mixture of thermal plus nonthermal sources by t_3 , while C is mostly a thermal source.

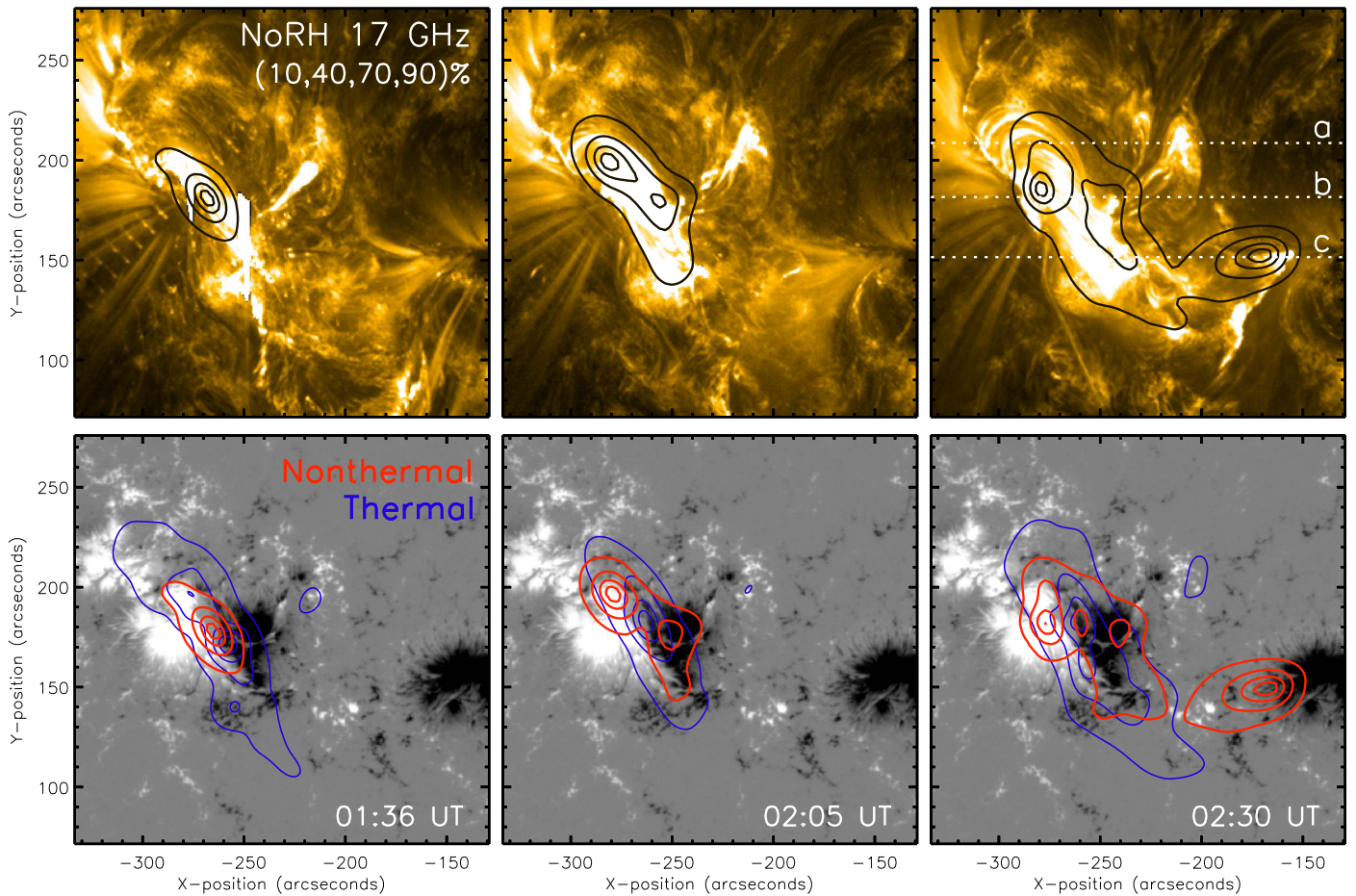


Figure 4. Locations of thermal and nonthermal electrons. Top panels: 17 GHz NoRH sources (black contours) on the *AIA* 171 Å images. Bottom panels: calculated 17 GHz f - f maps (blue contours) and the difference map (red contours) over the HMI longitudinal magnetogram. The blue and red contours are regarded as the thermal and nonthermal sources, respectively.

5. Thermal and Nonthermal Structure

In Figure 5, we plot the one-dimensional (1D) map profiles to see further details of the thermal and nonthermal structure and check possible issues regarding the intensity calibration and alignment that are critical for the interpretation of the thermal-component subtraction. The thick gray lines are the observed 17 GHz brightness temperature, and the dashed lines are the f - f emission computed with the EM(T) along the three slits (a to c) denoted in Figure 4. The f - f emission is computed at the original resolution of *AIA* (pixel size $0''.6$), and, as expected, there are variations from pixel to pixel and even missing values where the solution of the DEM inversion is not found. We convolve the DEM maps with a Gaussian beam of $10''$ in order to match the resolution of the NoRH maps at 17 GHz. After the beam convolution, the computed f - f intensity profiles are smooth, as shown in the figure.

The left column shows T_b profiles at the maximum of the first flare (t_1), where the single dominant peak is seen along all slits. There is so little thermal emission that the observed radio source is simply a nonthermal source lying over the PIL of the bipolar spot region. The middle column shows the T_b profiles at the intermission time (t_2), in which a thermal source is now centered above the PIL, similar in position to but narrower in width than the observed 17 GHz source. Upon subtraction of the thermal emission, we find that the remaining nonthermal emission (black solid lines) splits into two sources. We

interpret this structure as indicating that the nonthermal electrons are now present in newer positions further away from the PIL, whereas the nonthermal electrons initially above the PIL are now thermalized. In the third column (t_3), the same trend is seen on slit b, where the two nonthermal sources are even further separated. The additional splitting of the two nonthermal sources away from the PIL corresponds to the classic pattern of two-ribbon separation known from $H\alpha$ observations. Another interesting feature is the western nonthermal source B, which becomes prominent, particularly in slit c, by t_3 . While B has no thermal component, A has both thermal and nonthermal components. After the thermal component is subtracted from the observed 17 GHz brightness, B becomes even more prominent. In terms of nonthermal emission only, B is stronger than A at t_3 .

A cautionary remark would be appropriate here, since the above subtraction results are subject to the accuracy in positioning and calibration of the radio brightness. As a matter of fact, the two peaks of nonthermal sources separating away from the PIL are valid when the *AIA*-derived thermal source lies in the middle of the NoRH source. If the location of the NoRH source were off by $\sim 20''$ to either the east or the west so that the maximum T_b were close to that of T_b^T , an alternative interpretation would have resulted that one peak is mostly thermal while the other is nonthermal. Such a large misalignment is, however, impossible considering the fact that the locations of the sources are determined by matching the radio

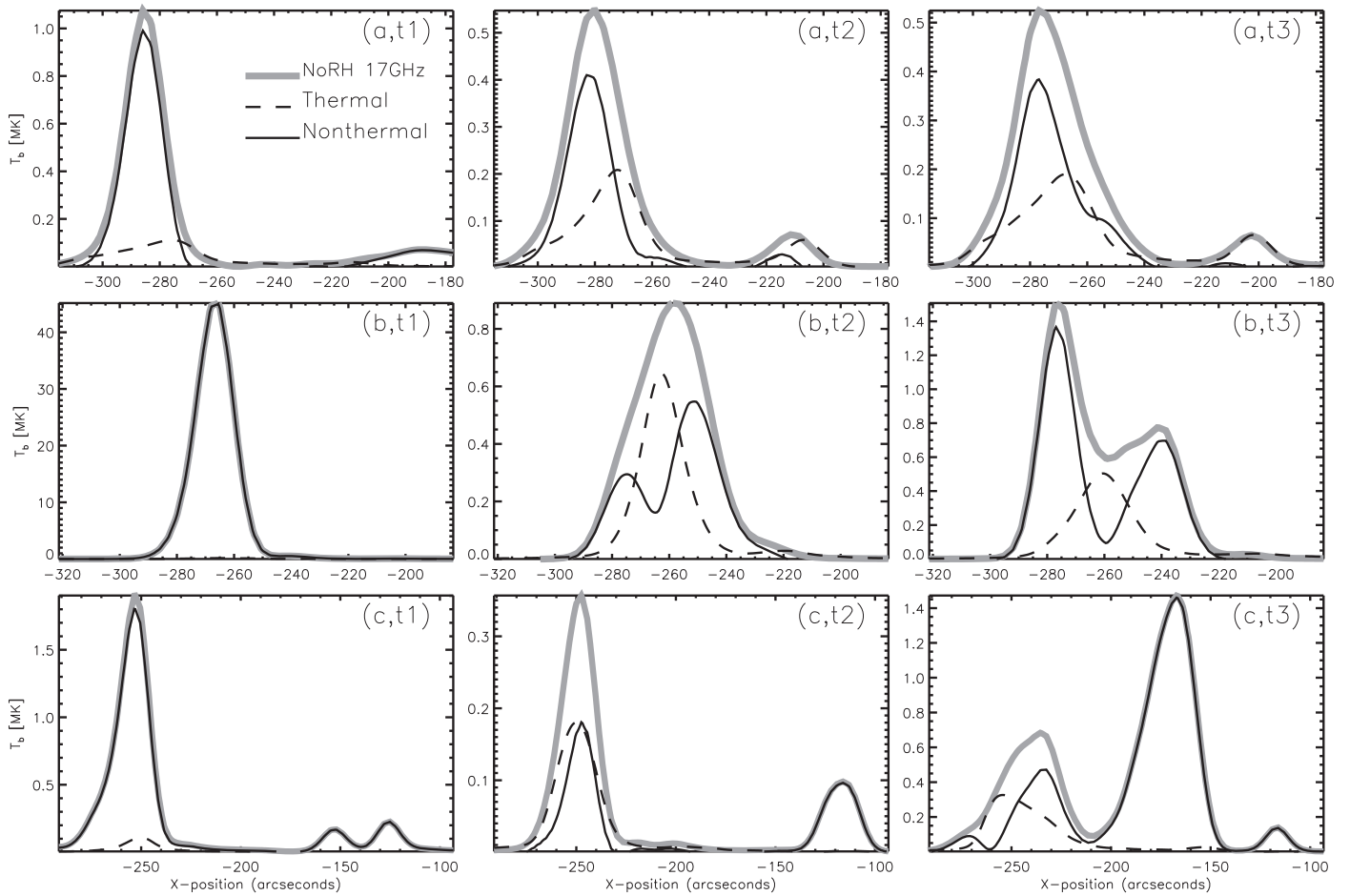


Figure 5. One-dimensional structure of the 17 GHz brightness temperatures: the NoRH (thick gray lines), thermal (dashed lines), and the difference taken as nonthermal (black solid lines) at the three time intervals (t_1 – t_3) and along the slits, a–c, denoted in Figure 4.

circular polarization measurements against the HMI magnetogram and the relative locations of the three NoRH sources matching those of EUV sources in position.

6. Temporal Evolution of Parameters

An alternative and maybe more robust method for identifying thermal and nonthermal sources would be to look at the temporal correlations between the observed fluxes and calculated thermal fluxes for individual sources. Such a test is performed in Figure 6, where the columns (left to right) show time profiles of the f–f flux, electron temperature, and EM, and the rows (top to bottom) show the three local sources A, B, and C (boxes as denoted in Figure 3). In the first column, the black lines are the 17 GHz f–f fluxes calculated from the *AIA* EUV, the thick gray lines are the corresponding flux from the *GOES* soft X-ray data, and the thin gray lines are the spatially resolved NoRH 17 GHz fluxes over the three local regions. The next two columns show the electron temperatures and EM for the three local sources, for which only the calculated quantities from the *AIA* and *GOES* are compared with each other.

We need to explain the obvious differences between the *AIA*-derived quantities and the *GOES*-derived ones. In the first column, the calculated f–f fluxes are generally lower than the observed NoRH fluxes, which is expected for the observed flux that consists of both thermal and nonthermal components. However, it came to our attention that the *GOES*-derived flux is much lower than the observed NoRH flux and even lower than

the *AIA*-derived local fluxes, despite the fact that the *GOES* data represent the contribution by the whole Sun. We believe this discrepancy occurs because *GOES* is more sensitive to higher-temperature plasma, while the *AIA* responds to a wide range of temperatures, including low temperatures. We will further demonstrate this point while investigating the temporal evolution of the temperatures (middle column) and the EM (right column) in the rest of this section.

To look at the temporal evolution of the fluxes, both the *AIA*- and *GOES*-derived fluxes show the trend of forming a thermal envelope under the observed 17 GHz flux. Any impulsive behaviors uncorrelated with this smooth thermal envelope can therefore be regarded as the contribution by the nonthermal emission. The dominantly high fluxes from A during the first flare indicate such nonthermal sources. The thermal flux gradually grows to dominate from 01:45 to 02:06 UT. The increase in 02:06 UT above the thermal flux must be related to the large-scale disturbances. Source B is a very weak thermal source, as is evident from its faint EUV emission, but it nonetheless shows an abrupt rise at 02:20 UT, which is still much lower than the observed flux level. Source B is therefore a nonthermal source. Source C shows a contrasting behavior: the *AIA*-derived flux closely reproduces the observed NoRH flux, indicating that C is mostly a thermal source except for a few periods.

In the middle column, the *GOES*-derived electron temperature (gray lines) has a single value at a time, but the

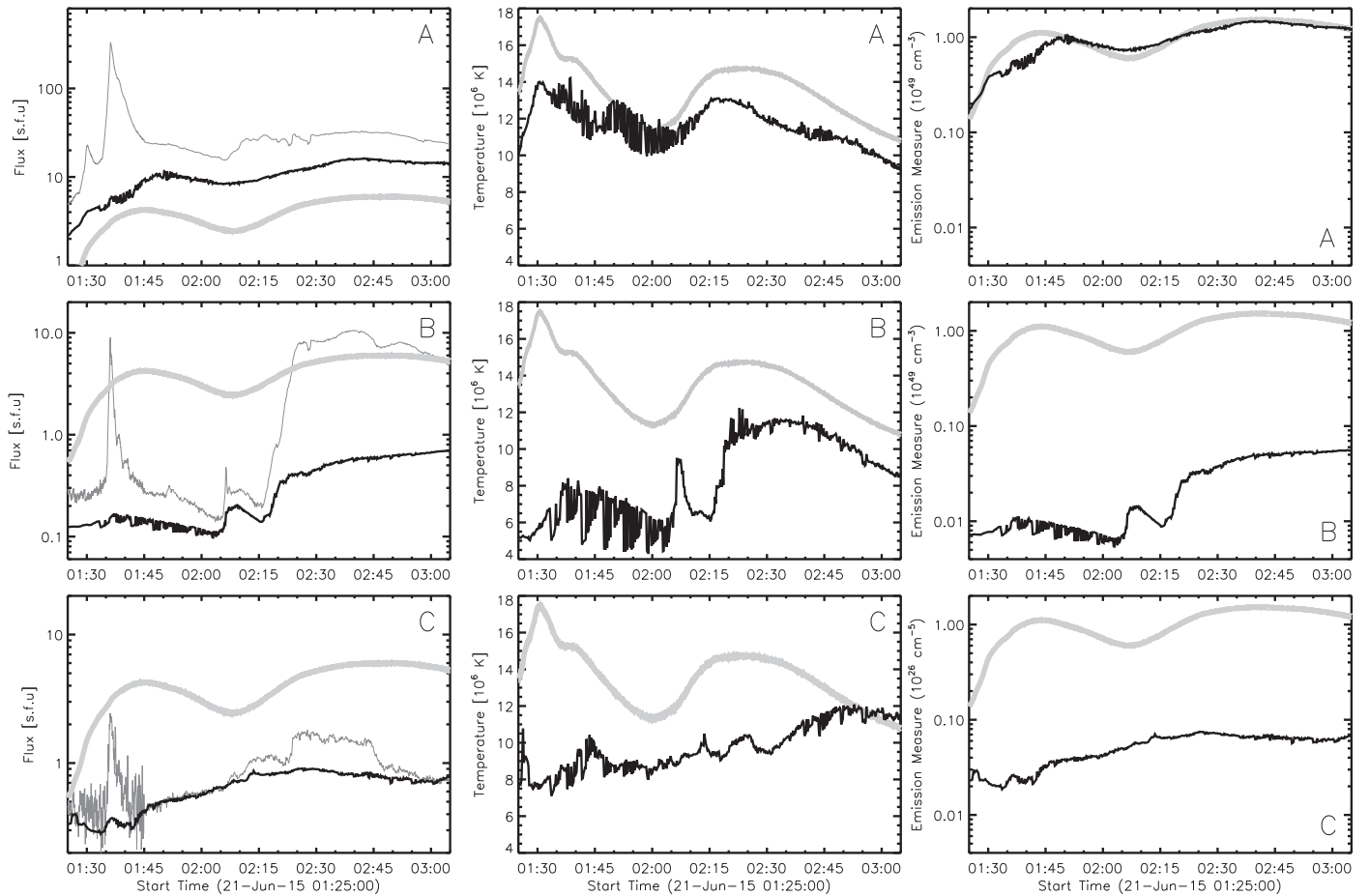


Figure 6. Temporal evolution of 17 GHz flux, T , and EM in the three local microwave sources: A (top panels), B (middle panels), and C (bottom panels). In the first column, the observed NoRH flux (thin gray lines), *GOES*-derived f-f flux (thick gray lines), and *AIA*-derived f-f flux (black lines) are shown. The second and third columns show temperatures and EMs, respectively. *GOES*-derived quantities are in gray, and *AIA*-derived quantities are in black.

AIA-derived electron temperatures (black lines) refer to the average temperatures weighted by the EM over all temperature intervals. In A, the *AIA*-derived temperature evolves similar to the *GOES* temperature but does not reach the highest *GOES*-derived temperatures. We interpret this as due to the different temperature response of the two instruments. Source B has an instantaneous temperature rise at 02:05 UT that quickly cools down and another impulsive rise at 02:20 UT that stays afterward. The latter must be associated with the acceleration of nonthermal electrons and their trapping within B. In contrast, C shows a monotonic increase of temperature regardless of the flares, which implies that C does not directly respond to the flare energy input. Both EUV and EM maps suggest that C passively receives thermal energy from A through a magnetic channel. It must be that A steadily releases thermal energy in spite of the impulsive flare heating inside itself.

The right column shows the total EM integrated not only over the entire temperature range but over each source area. We note that for A (top panel), the *AIA*-derived EM (black line) follows the *GOES*-derived EM (gray line) very closely. This agreement is rather good in magnitude and temporal evolution, considering that the *GOES*-derived EM is supposed to represent not only A but the whole Sun. A possible interpretation is that A was the only dominant source on the whole Sun at those high temperatures to which *GOES* is

sensitive, and the *GOES*-based EM came out comparable to the *AIA*-based EM of A. Source B obviously has very low EMs, as it is practically an EUV-void region. This tells us that B is ideal for high-energy electrons to survive under Coulomb collisions (Brown 1972). It nonetheless shows a rapid temperature increase at 02:07 UT, and again at 02:20 UT, which implies the primary energy release and associated chromospheric evaporation at those times. In C, the EM evolves uncorrelated with the flares in that it rather monotonically increases throughout the flares.

We briefly discuss the possibility that contribution from high-temperature plasma might be underestimated due to the finite temperature sensitivity of each instrument. The fact that *GOES* is sensitive to slightly higher temperatures than *AIA* implies that, for hot sources, *AIA* may underestimate EM more than *GOES*, and, for hotter sources, even *GOES* may underestimate EM. It is, however, f-f flux rather than EM itself that is more important for our purpose. In this regard, we note that the flux has a temperature dependence in the form of $EM(T) T^{-1/2}$ (Equation (1) and $T_b \approx \tau T$). Fortunately, $EM(T)$ tends to decrease above a certain high temperature (say, ≥ 30 MK) most of the time. This trend, together with the $T^{-1/2}$ dependence, makes the contribution from very hot plasma to the f-f flux less important. We thus believe that *AIA*'s temperature sensitivity is suitable for the estimation of the f-f flux.

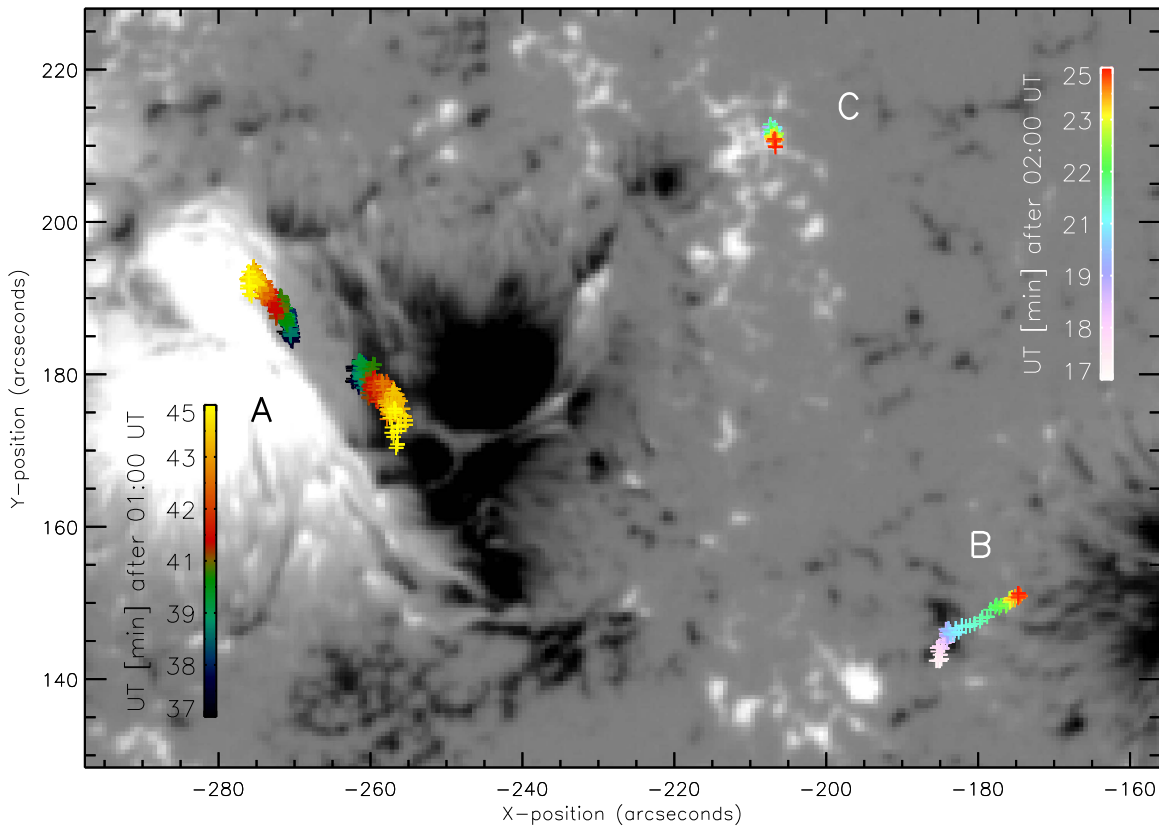


Figure 7. Locations of the center-of-mass of the 17 GHz NoRH sources on the HMI longitudinal magnetogram. Motions of the two peaks of A are plotted with the color table shown on the left-hand side, and those of B and C are plotted with the color table on the right-hand side.

7. Conclusion

We have derived the EM information from the *SDO/AIA* (E)UV lines and use it in the analysis of the composite solar flare, SOL2015-06-21T01:42 and SOL2015-06-21T02:36, to identify three distinctive sources in terms of the plasma heating and nonthermal electron acceleration. We summarize the major findings in Figure 7, in which we mark the center-of-mass locations of the 17 GHz brightness of the three local sources with time-stamped colors. These locations are traced for two separate time intervals, because B and C became active much later than A.

Source A is the main source located within the bipolar spot, which produced the initially short-lived impulsive flare and then a second weak gradual flare. Through these two consecutive flares, both thermal and nonthermal sources gradually expand, which can be regarded as the Neupert (1968) effect in both time and space. However, the thermal and nonthermal particles appear in subtly different locations. While the nonthermal source expands in width across the PIL, the middle part of the nonthermal source weakens and turns into a thermal source. As a result, the nonthermal source appears to split into two peaks, as shown in Figure 5 by the thin black line along line b exhibiting a single peak at t_1 and two peaks at t_2 and t_3 . Figure 7 clarifies that one of those two nonthermal peaks lies in the positive magnetic polarity region and the other in the negative polarity region and that the two peaks move away from the PIL with time. This phenomenon is consistent with the well-known $H\alpha$ ribbon separation phenomenon regarded as evidence for the standard solar flare reconnection model (e.g., Forbes 2000).

Source B is another magnetically confined source for nonthermal acceleration, as it shows an impulsive rise of microwave radiation and motion of the centroid of the 17 GHz emission. A difference between B and A is that A shows extended flare activity. This source is very weak in EUV, suggesting that the thermal particles are depleted, allowing nonthermal electrons to survive longer against Coulomb collisions. As a result, B is almost entirely nonthermal and exhibits a systematic motion similar to that of A. It seems appropriate to compare B with the so-called “cold flares” that emit hard X-rays without accompanying soft X-rays, regarded as evidence for electron acceleration without thermal heating (Fleishman et al. 2011). A similarity between B and the cold flares is that the presence of nonthermal electrons is implied by the significant intensity at 17 GHz, and the absence of thermal electrons is indicated by the very weak EUV emission detected by *AIA*. We found, however, that the faint EUV emission is due to a small EM that is hotter than that of C. This implies that either B does not fall into the category of cold flares or the idea of cold flares needs to be refined to accommodate properties such as those of B.

Source C is a counterexample to B in that it is a thermal source rich in EUV and poor in microwaves. Although such a source must actually be common, this study revealed a couple of properties yet unknown: its temperature and EM evolve monotonically as if they are independent of the flare, and it shows no systematic motion. The latter is explicable as with the thermal source in A; a thermal source can be more static, as it does not directly rely on magnetic connection. This explains why the temperature and EM variation in C do not respond to the primary energy release. Source C may be a rare example of

a passive receiver of thermal energy from a thermal reservoir through a magnetic channel, as identified from EUV images and DEM analysis.

The flux and EM in B and C are an order of magnitude weaker than those in A. They could nevertheless be detected thanks to the excellent sensitivity of the NoRH and spatial resolution of the *SDO/AIA*. It is remarkable that these two independent instruments, one in space and the other on the ground, could simultaneously detect the subtle interplay between the thermal heating and nonthermal electron acceleration within a complex active region. This demonstrates how the combination of *SDO/AIA* and NoRH observations can help in understanding the nonthermal particle acceleration and thermal heating in solar flares.

We thank the NASA *SDO* team for HMI and *AIA* data. HMI and *AIA* are instruments on board *SDO*, a mission for NASA's Living with a Star program. This work was carried out by the joint research program of the Institute for Space-Earth Environmental Research, Nagoya University. J.L. thanks KOFST for the support under the Brain Pool program. S.W. was supported by an AFOSR WoW travel grant and LRIRs 14RV14COR and 17RVCOR416. J.J. was supported by NASA grant NNX13AG13G. C.L. is supported by NASA grants NNX13AF76G and NNX16AF72G. We also thank the Korea Astronomy and Space Science Institute for the R&D program, Development of a Solar Coronagraph on International Space Station (Project No. 2017-1-851-00), supervised by the Ministry of Science, ICT, and Future Planning.

ORCID iDs

Jeongwoo Lee  <https://orcid.org/0000-0002-5865-7924>
 Stephen M. White  <https://orcid.org/0000-0002-8574-8629>

Ju Jing  <https://orcid.org/0000-0002-8179-3625>
 Chang Liu  <https://orcid.org/0000-0002-6178-7471>
 Jongchul Chae  <https://orcid.org/0000-0002-7073-868X>

References

- Asplund, M., Grevesse, N., Sauval, A. J., & Scott, P. 2009, *ARA&A*, **47**, 481
 Benka, S. G., & Holman, G. D. 1992, *ApJ*, **391**, 854
 Boerner, P., Edwards, C., Lemen, J., et al. 2012, *SoPh*, **275**, 41
 Brown, J. C. 1972, *SoPh*, **25**, 158
 Cheung, M. C. M., Boerner, P., Schrijver, C. J., et al. 2015, *ApJ*, **807**, 143
 Dulk, G. A. 1985, *ARA&A*, **23**, 169
 Dulk, G. A., & Marsh, K. A. 1982, *ApJ*, **259**, 350
 Feldman, U. 1992, *PhyS*, **46**, 202
 Fleishman, G. D., Kontar, E. P., Nita, G. M., & Gary, D. E. 2011, *ApJL*, **731L**, 19
 Fludra, A., & Schmelz, J. T. 1999, *A&A*, **348**, 286
 Forbes, T. G. 2000, *JGR*, **105**, 23153
 Gary, D. E., Fleishman, G. D., & Nita, G. M. 2013, *SoPh*, **288**, 549
 Gary, D. E., & Hurford, G. J. 2004, *ASSL*, **314**, 71
 Jing, J., Liu, R., Cheung, M. C. M., et al. 2017, *ApJ*, **842L**, 18
 Kosugi, T., Dennis, B. R., & Kai, K. 1988, *ApJ*, **324**, 1118
 Krücker, S., & Battaglia, M. 2014, *ApJ*, **780**, 107
 Krücker, S., Saint-Hilaire, P., Hudson, H. S., et al. 2015, *ApJ*, **802**, 19
 Lemen, J. R., Title, A. M., Akin, D. J., et al. 2012, *SoPh*, **275**, 17
 Melrose, D. B. 1980, *Plasma Astrophysics, I and II* (New York: Gordon and Breach)
 Neupert, W. 1968, *ApJ*, **153L**, 59
 Pesnell, W. D., Thompson, B. J., & Chamberlin, P. C. 2012, *SoPh*, **275**, 3
 Phillips, K. J. H., Sylwester, J., Sylwester, B., & Kuznetsov, V. D. 2010, *ApJ*, **711**, 179
 Saint-Hilaire, P., Krucker, S., Christe, S., & Lin, R. P. 2011, *ApJ*, **696**, 941
 Schmelz, J. T., Reames, D. V., von Steiger, R., & Basu, S. 2012, *ApJ*, **755**, 33
 Schonfeld, S. J., White, S. M., Henney, C. J., Arge, C. N., & McAteer, R. T. J. 2015, *ApJ*, **808**, 29
 White, S. M., Thomas, R. J., Brosius, J. W., & Kundu, M. R. 2000, *ApJ*, **534**, 203
 Widing, K. G., & Feldman, U. 2001, *ApJ*, **555**, 426